Optimization of in-line phase contrast particle image velocimetry using a laboratory x-ray source

I. Ng, D. M. Paganin, and A. Fouras

Related Articles

Angle-resolved environmental X-ray photoelectron spectroscopy: A new laboratory setup for photoemission studies at pressures up to 0.4 Torr
Rev. Sci. Instrum. 83, 093112 (2012)

Quasi-monochromatic field-emission x-ray source
Rev. Sci. Instrum. 83, 094704 (2012)

Synchrotron-based coherent scatter x-ray projection imaging using an array of monoenergetic pencil beams
Rev. Sci. Instrum. 83, 095114 (2012)

The x-ray source application test cassette for radiation exposures at the OMEGA laser
Rev. Sci. Instrum. 83, 10E136 (2012)

Glancing angle Talbot-Lau grating interferometers for phase contrast imaging at high x-ray energy
Appl. Phys. Lett. 101, 091108 (2012)
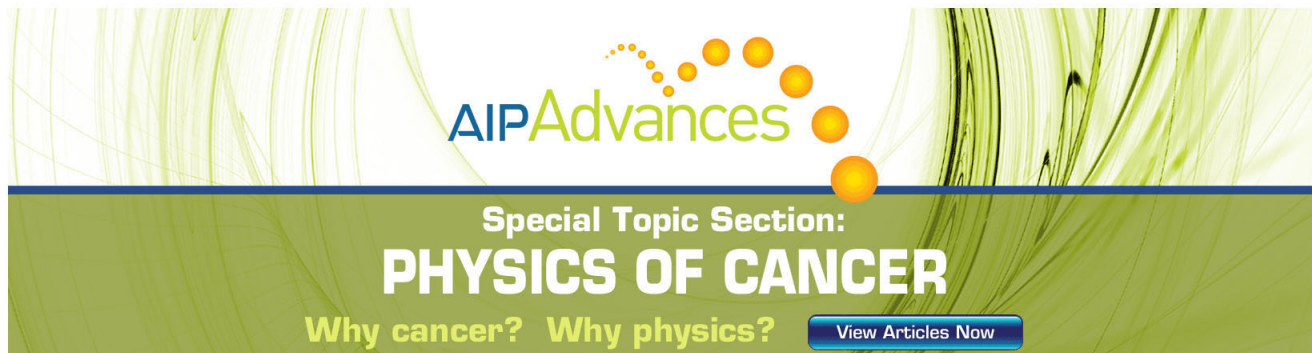
Additional information on J. Appl. Phys.

Journal Homepage: http://jap.aip.org/

Journal Information: http://jap.aip.org/about/about_the_journal

Top downloads: http://jap.aip.org/features/most_downloaded

Information for Authors: http://jap.aip.org/authors

Optimization of in-line phase contrast particle image velocimetry using a laboratory x-ray source

I. Ng,[1] D. M. Paganin,[2] and A. Fouras[1]
[1]*Division of Biological Engineering, Monash University, Clayton, Victoria 3800, Australia and Department of Mechanical and Aerospace Engineering, Monash University, Clayton, Victoria 3800, Australia*
[2]*School of Physics, Monash University, Clayton, Victoria 3800, Australia*

Phase contrast particle image velocimetry (PIV) using a laboratory x-ray microfocus source is investigated using a numerical model. Phase contrast images of $75\,\mu$m air bubbles, embedded within water exhibiting steady-state vortical flow, are generated under the paraxial approximation using a tungsten x-ray spectrum at 30 kVp. Propagation-based x-ray phase-contrast speckle images at a range of source–object and object–detector distances are generated, and used as input into a simulated PIV measurement. The effects of source-size-induced penumbral blurring, together with the finite dynamic range of the detector, are accounted for in the simulation. The PIV measurement procedure involves using the cross-correlation between temporally sequential speckle images to estimate the transverse displacement field for the fluid. The global error in the PIV reconstruction, for the set of simulations that was performed, suggests that geometric magnification is the key parameter for designing a laboratory-based x-ray phase-contrast PIV system. For the modeled system, x-ray phase-contrast PIV data measurement can be optimized to obtain low error (<0.2 effective pixel of the detector) in the system with magnification lying in the range between 1.5 and 3. For large effective pixel size ($>15\,\mu$m) of the detector, high geometric magnification (>2.5) is desired, while for large source size system (FWHM $> 30\,\mu$m), low magnification (<1.5) would be suggested instead. The methods developed in this paper can be applied to optimizing phase-contrast velocimetry using a variety of laboratory x-ray sources. © *2012 American Institute of Physics*. [http://dx.doi.org/10.1063/1.4757407]

I. INTRODUCTION

Absorption based x-ray imaging has been used for over a century.[1] This attenuation-based imaging method is widely used for clinical imaging to investigate bone fractures[2] and, especially with the use of suitable contrast agents, can be used to image x-ray-transparent structures, such as blood vessels, tumors, and cancers.[3] The disadvantage of absorptive x-ray imaging is that at hard-x-ray energies any weakly absorbing tissues such as red blood cells, alveoli, and bacteria are difficult to image.[4,5]

As an alternative to use of contrast agents, phase contrast may be employed. We restrict consideration to propagation-based phase contrast, in which traverse phase variations of an optical field over the exit-surface of an illuminated weakly absorbing object are converted to intensity variations over the surface of a position-sensitive detector, via free-space propagation of the field from the object to the detector. Early investigations of x-ray phase-contrast imaging include papers by Snigirev *et al.*,[6] Cloetens *et al.*,[7] Nugent *et al.*,[8] and Wilkins *et al.*[9] The field of propagation-based phase contrast with short wavelength x-rays has since become an important and widely utilized visualization method for weakly x-ray absorbing objects—see, e.g., the recent review by Gureyev *et al.*[10]

Independently of the above advances, particle image velocimetry (PIV) is a well-established flow measurement technique that has been widely used in fluid mechanics over the last two decades.[11] In conventional PIV, particles are seeded into transparent flows as tracers, with a visible-light laser generally being used as a light-source for illuminating the particles, which are then imaged in side-scatter.[12] The displacement of the particles in sequential frames is calculated statistically, with the modal value of the local cross-correlation used to determine the velocity of the flow.[13]

Combining x-ray phase contrast imaging with the PIV technique, one can replace the visible-light laser by an x-ray light source to investigate an optically opaque system.[14,15] In these approaches, the movement of a phase contrast speckle pattern has been shown to faithfully represent the motion of the particles that create that speckle pattern.[16,21] The speckle pattern, from the phase-contrast image of cellular tissues such as alveoli and red blood cells, takes the place of seeding particles in x-ray PIV and is called x-ray phase contrast velocimetry. In the same fashion as in x-ray PIV, the cellular movement can be estimated by the displacement of the local speckle pattern, removing the requirement to use additional tracer particles.[16]

X-ray phase contrast velocimetry can be used for detecting many important biological flows such as blood flow, lymphatic flow, and airflow in the respiration system.[15,17] The combination of these two techniques is clinically valuable, as many cellular tissues that are invisible in conventional x-ray imaging can now be visualized by the speckle pattern of the tissues. Direct velocity measurement from the temporally evolving speckle patterns increases the accuracy in estimating the biological flows or the movement of organs when compared to conventional PIV. Experimental studies using

synchrotron sources have shown that the combined technique can be used to provide *in vivo* and *in vitro* blood flow measurement,[16,18] and three-dimensional measurement of blood-flow in optically opaque systems.[14,19,20] The same technique can also be used to measure lung tissue movement from the speckle pattern of alveoli,[15,21] which can be used to help determining lung function.

The use of synchrotron sources, both for x-ray phase contrast in general and for x-ray phase-contrast velocimetry in particular, has a main advantage over laboratory-based sources of a high number of x-ray photons per unit area per unit time (termed "photon flux" henceforth), reducing the required exposure time. However, it would be highly desirable to be able to employ laboratory sources due to their greater availability, ability to be located in or near medical facilities, and significantly reduced overall cost.[9]

The main obstacle for laboratory source phase-contrast imaging, in the context of velocimetry, is the limited photon flux of the x-rays from a laboratory source. Key works on laboratory-based coherent x-ray imaging include in-line imaging using a microfocus x-ray source,[9] x-ray interferometry,[4,23] grating interferometry,[24,25] and x-ray phase contrast using an inverse-Compton source.[22] For the propagation-based method, the spatial coherence of a polychromatic source is sufficient to provide phase contrast;[9,26,27] for associated theoretical studies, see the review by Gureyev *et al.*[10] together with primary references therein. The simplicity of this imaging method implies that in-line phase-contrast imaging using microfocus x-ray sources has the potential for clinical application. These observations are the principal reason for pursuing this means of x-ray phase contrast in the present investigation.

The remainder of the paper is structured as follows. Section II gives a brief review of the underpinning theoretical background on x-ray propagation-based phase contrast imaging (Sec. II A) and particle image velocimetry (Sec. II B). Section III presents our theoretical model for x-ray phase contrast velocimetry using a laboratory source, with corresponding numerical results in Sec. IV. Our conclusions are presented in Sec. V.

II. BACKGROUND THEORY

Here, we briefly outline the review of some relevant background theory for in-line x-ray phase contrast particle image velocimetry using a laboratory x-ray source. More specifically, Sec. II A outlines the relevant x-ray phase contrast imaging background theory, while in Sec. II B we sketch the relevant velocimetry background theory.
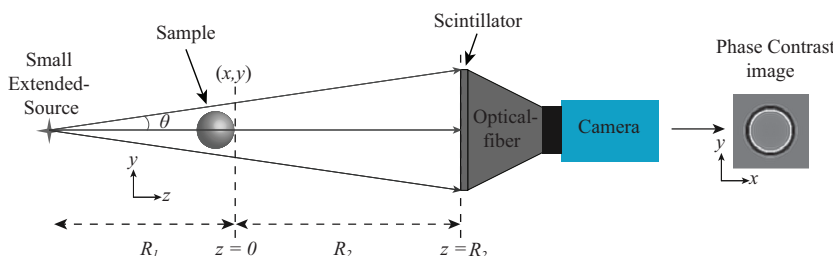
A. In-line x-ray phase contrast imaging

The key principles of in-line x-ray phase contrast imaging are illustrated in Fig. 1. Here, x-rays from a small extended-source illuminate a weakly absorbing sample. Imaging using the field at the exit-surface $z = 0$ has two key disadvantages: (1) its transverse intensity variations are too weak on account of the weakly absorbing nature of the object, and (2) the image needs to be magnified. Both disadvantages are solved by placing a position-sensitive detector at a sufficiently large distance R_2 downstream of the sample: (1) Fresnel diffraction converts the transverse phase variations over the plane $z = 0$ into detectable intensity variations (i.e., propagation-based phase contrast) over the plane $z = R_2$; and (2) use of a small extended source gives a magnified image over the plane $z = R_2$.[9]

The formalism for the above is as follows. Consider a single-material object with projected thickness $T(x, y)$, where x, y denote Cartesian coordinates in a plane perpendicular to the optic axis z. When a z-directed monochromatic plane wave with intensity I_0 and wavenumber k is normally incident on such a single-material sample, the spatial part of the complex disturbance at the exit-surface $z = 0$ of the sample is given in the projection approximation by $\psi(x, y, z = 0) = \sqrt{I_0}\exp[-(\frac{1}{2}\mu + i\delta k)T(x, y)]$.[29] Here, δ is the refractive index decrement and μ is the linear attenuation coefficient. The propagation-based phase contrast at distance $z = R_2$ (see Fig. 1) is obtained using the angular-spectrum formalism for forward-propagating monochromatic scalar wave fields:[29]

$$\psi(x, y, z = R_2) = \mathcal{F}^{-1}\{\exp(iR_2\sqrt{k^2 - k_x^2 - k_y^2}) \times \mathcal{F}[\psi(x, y, z = 0)]\}, \quad (1)$$

where $\mathcal{F}$ and $\mathcal{F}^{-1}$ are the Fourier transform with respect to x, y and the corresponding inverse Fourier transform, with k_x and k_y being the Fourier space coordinates corresponding to the Cartesian coordinates x, y.

For a polychromatic source, the resulting intensity $I(x, y, z = R_2) = |\psi(x, y, z = R_2)|^2$ may be averaged using the spectral sum:[9]

$$I_{poly}(x, y, z = R_2) = \int S(\lambda)I(x, y, z = R_2, \lambda)d\lambda, \quad (2)$$

where $S(\lambda)$ is the spectral weight for each individual wavelength λ.

For a microfocus x-ray source, the wavefront is essentially spherical. Provided that the spherical waves are paraxial at each point on both the entrance surface of the sample

FIG. 1. Schematic of extended-source in-line phase contrast imaging. X-rays emitted from a small extended-source travel along the optic axis z with a beam divergence θ. R_1 and R_2 are the source-object distance and object-detector distance, respectively. An absorption contrast image of the object corresponds to the exit-surface $z = 0$. A phase contrast image corresponds to the detector plane $z = R_2$.

and at each pixel of the detector, the above results for plane-wave illumination may be transformed into the corresponding formulae for point-source illumination using the Fresnel scaling theorem.[29]

Another effect that must be taken into account to properly model laboratory-source x-ray phase-contrast imaging is the fact that the diffraction pattern from a source is blurred due to "penumbral blurring" (source-size blurring). This results in blurring of the image via convolution with an incoherent point-spread function with width $\Delta \approx D(R_2/R_1)$, where R_1 is the distance from the source to the sample. This effect was incorporated into our simulations via convolution with a two-dimensional Gaussian function. Note that a trade-off is evident here: R_2 must be not only sufficiently large to have sufficient propagation-induced phase contrast but also sufficiently small for the effects of penumbral blurring to not overly degrade the image.

B. Particle image velocimetry

PIV is a well-established technique that has been used to measure fluid velocity fields for over two decades.[11] For PIV analysis, images of particles are divided into a grid of interrogation windows (see Fig. 2). Consider an image of a group of particles with intensity distribution $I(x,y)$ initially, with the particles then moving before being captured by the second image with intensity distribution $I'(x,y)$. To determine the local displacement at each point in the image, one can calculate the cross-correlation function $R_{II'}$ of the image pair I and I' using a complex conjugate multiplication:[12]

$$R_{II'} = \mathcal{F}^{-1}[\mathcal{F}(I) \cdot \mathcal{F}(I')^*]. \tag{3}$$

Both images I and I' are divided into a grid of interrogation windows. Applying Eq. (3) for each window, a map of correlation peaks is determined for each image pair at each window. The location of each peak indicates the mean shifting of the particles in the individual interrogation window. If the time interval between the image pairs is known, the modal value of velocity of the particles can be estimated for each interrogation window, by dividing the displacement at that
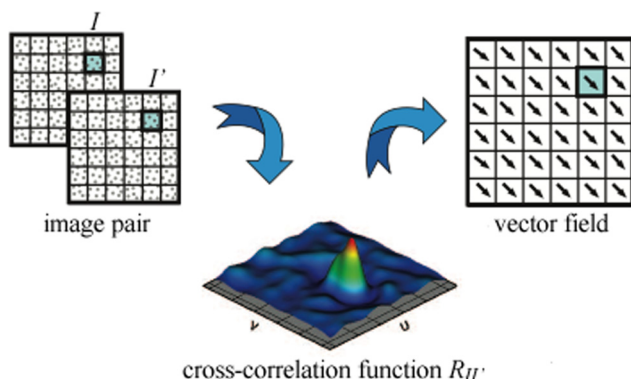

FIG. 2. Schematic diagram for PIV analysis. The image pair on the left is divided into a grid of interrogation windows. The cross-correlation for each peak is integrated, with the location of the peak providing an estimate of the average displacement of particles in the window. The peaks of all interrogation windows visualize the vector field of the image pair. Adapted from Ref. 15.

window by the known time interval. Note also that the spatial resolution of the resulting reconstructed velocity field can be extended beyond the one-pixel level using a three-point interpolation of the cross-correlation peak.[12] For further information regarding the validity and limitations of the PIV algorithms implemented in this study, we refer the reader to Fouras *et al.*[30,31] together with references therein.

III. THE MODEL

To determine the optimization of R_1 and R_2 for phase contrast velocimetry, a simulation model for in-line phase-contrast imaging of mouse lungs was performed. The alveoli were simulated by air-filled hollow spheres surrounded by water. Alveolar diameters in mice are typically in the range of 38 to 80 μm; the density of a mouse lung is approximately 5500 alveoli/mm^3.[32] For our study, the pixel size of the model was set to 5 μm, which was in the range of the physical pixel size of CCD cameras. Note that to be able to generate phase-contrast images with appropriate resolution for the range of geometries used in this study, the diameter of spheres in the simulation should be sufficiently large to yield a detectable scattered intensity variation, in which the variation can be resolved by the 5 μm pixels. The sphere diameter was chosen to be 75 μm. The chosen sphere diameter satisfies this criterion, as will be evident from the simulation results presented later in this paper. These spheres were randomly placed in a three-dimensional model of the sample. The maximum physical depth of the simulated sample was 10.2 mm, which had an average density of 3300 spheres/mm^3. The simulated sample was then projected as a two-dimensional image of thickness function with physical dimensions of 10.2×10.2 mm^2. This image was used to calculate a given phase-contrast image using the squared modulus of Eq. (1). A second image was generated by displacing each sphere according to a numerical vortical flow. A vortical flow was chosen because in such a vector field a range of displacement magnitude is represented in all directions. The center of rotation of the flow was arbitrarily located at the center of the image, with a rigid rotation of 8 mrad between temporally consecutive images. The original image and the second image form an image pair of simulated lung motion. The above steps are summarised in the top left portion of the flowchart in Fig. 3; the whole flowchart summarizes all key aspects of the model, as presented in this section.

Next, the effects of having a non-monochromatic spectrum needed to be taken into account. The polychromatic spectrum $S(\lambda)$ in Eq. (2) was simulated using the software package x-ray Oriented Programs (XOP).[33] A tungsten x-ray tube at 30 kVp was selected as the source in the spectrum simulation. On the other hand, to evaluate $\psi(x, y, z = 0)$ in Eq. (1), the values of the refractive index decrement δ and the linear attenuation coefficient μ were required. Both values were determined from the National Institute of Standards and Technology (NIST) database. For the water-air interface at 30 kVp, $\delta = 2.35 \times 10^{-6}$ and $\mu = 37.44$ m^{-1}. Using the two images as thickness functions under the projection approximation, and applying Eq. (1) for the free-space propagation with the indices δ and μ calculated, the phase-
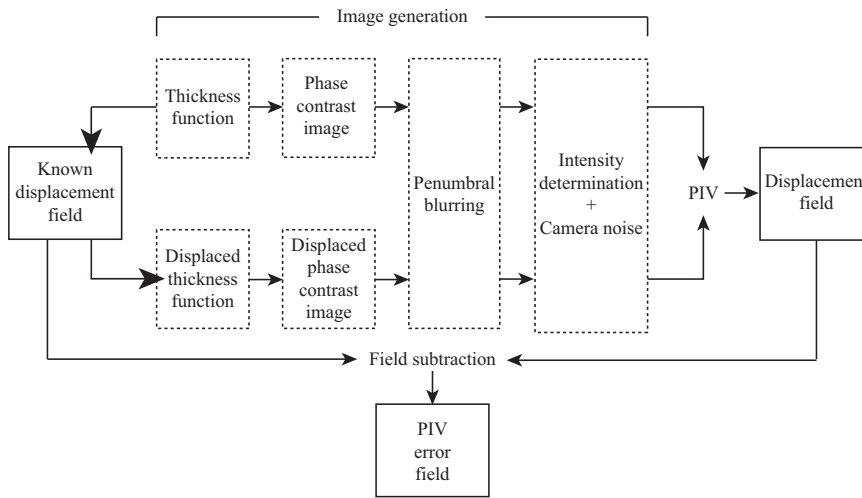
FIG. 3. Schematic flow chart of the simulation model. Dash boxes indicate the process of phase-contrast image generation, and solid boxes indicate the process for PIV analysis. Image pairs are generated according to a known displacement vector field. PIV is then performed on the image pair to calculate the image displacement vector field. PIV accuracy is determined by the error between the two displacement fields.

contrast images of the simulated sample were obtained for a selected range of R_1 and R_2 distances. Note that the input distance R_2 was replaced by R_2/M prior the running of the simulation, in accord with the Fresnel scaling theorem.[29] Penumbral blurring by an amount $\Delta \approx D(R_2/R_1)$ was incorporated via convolution with a two-dimensional Gaussian. The final intensity of the images was adjusted according to the individual distance R_1 following the inverse square law. Poisson noise was added to the images as a function of the intensity of the images to simulate counting statistics, while Gaussian noise was added at the final stage to simulate detector read-out noise, assuming the detector has a signal-to-noise ratio (SNR) of 3000 to 1 (i.e., 70 db, see Fig. 4). Note that this value of SNR is representative of existing commercially available cameras.

In this work, the detected phase contrast κ is defined as the ratio of the FWHM of the image intensity histogram relative to the intensity saturation level of the camera:

$$\kappa = \frac{\text{FWHM}}{I_{saturation}} \times 100\%. \qquad (4)$$

This measure of contrast is natural for the x-ray speckle-fields which form the input data for laboratory-source x-ray phase contrast velocimetry. Note that the more common contrast measure, given by the Michelson visibility,[34] is not appropriate for speckle fields since the global intensity maxima and minima, needed for the Michelson visibility, will be unduly influenced by extreme outliers in the spatially random intensity distribution, hence our adopted measure based on the FWHM of the image intensity histogram. Note also that the dimensionless contrast measure κ, being detector dependent, does not describe a fundamental property of the optical speckle field *per se*, but rather a property of the field-plus-detector system.

PIV analysis was performed for each simulated phase-contrast image pair. The 2048 × 2048 pixel images were divided into grids of 17 × 17 interrogation windows. Using Eq. (3), the correlation peak for each window was obtained, which indicates the average transverse displacement within the individual window. A displacement field of 17 × 17 vectors was obtained for each image pair. The physical size of

the window was 0.6×0.6 mm^2; this physical size was kept constant at all binning levels.

To determine the velocimetry reconstruction accuracy, a known numerical vortical displacement field was generated (Fig. 5). Each displacement field obtained from simulated image pairs was subtracted from this vortical displacement field to obtain an error-map of 17 × 17 vectors. The standard deviation of the magnitude of these error vectors (PIV-error) was defined as $= N\sqrt{\sum_i \sum_j |V_{IN}^{ij} - V_{OUT}^{ij}|^2}$, where the normalization constant N is given by $N = 1/\sqrt{\sum_i \sum_j |V_{IN}^{ij}|^2}$,
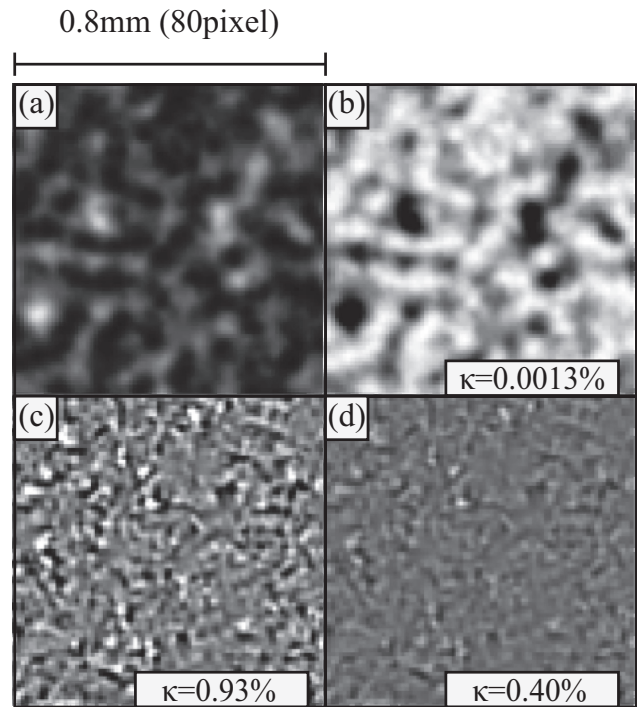
0.8mm (80pixel)

FIG. 4. Simulated images, 0.8 mm × 0.8 mm, of 21 540 air-filled hollow spheres with 75 μm diameter, pixel size of the image is 10 μm. (a) Projected thickness function; (b) contact intensity at $z = 0$ m; (c) projected phase contrast image at $z = 1$ m; (d) projected phase-contrast image at the same distance with noise. From the simulation, the phase-contrast image has contrast of about 300 times more than that of the exit-surface contrast. The detected contrast level κ (see Eq. (4)) of the contact image is 0.0013% while that of the phase-contrast image is 0.40%. Note that in panels (b), (c), and (d) the intensity has been stretched across the full dynamic range of the image.
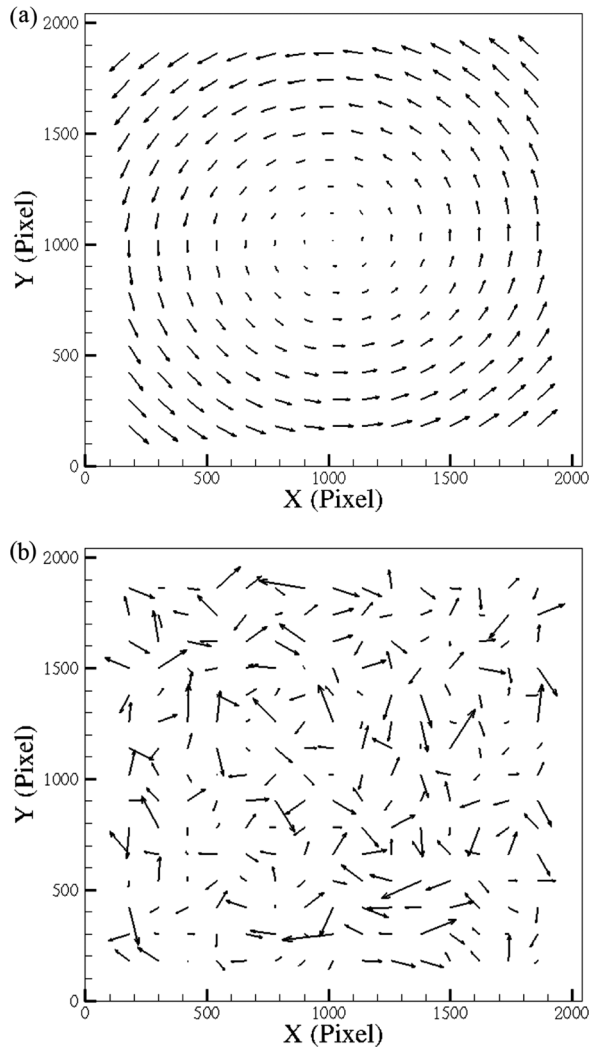
FIG. 5. (a) Displacement field of the spheres from PIV analysis; (b) PIV-error field from the subtraction of the two fields. The standard deviation of the magnitudes of the error field indicates the PIV-error of the phase-contrast image; note that the error field shown above is rescaled by a factor of 100 relative to the displacement field.
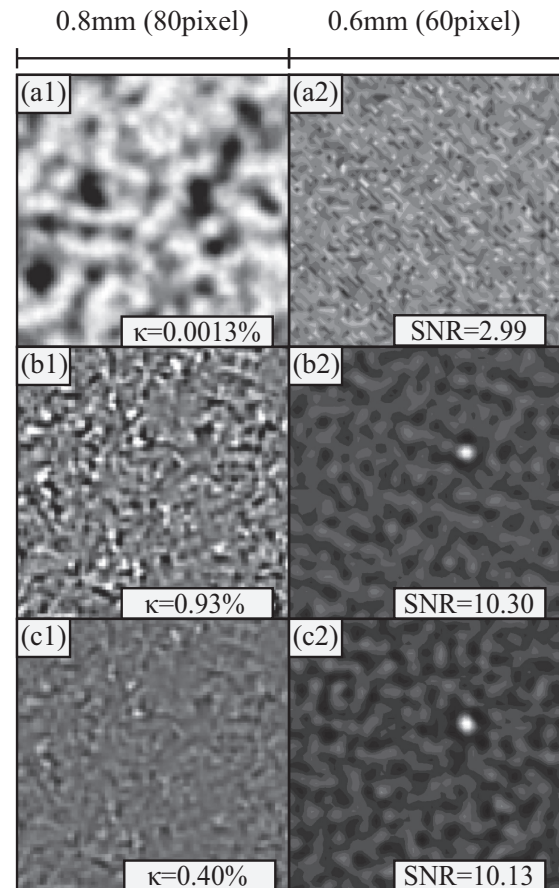

FIG. 6. Left column: Images from Figs. 4(b)–4(d); right column: correlation functions of the corresponding image. (a) Contact intensity at $z = 0$ m; (b) phase contrast intensity at $z = 1$ m; (c) phase contrast image at the same distance with noise. Note that in panels (a1), (b1) and (c1) the intensity has been stretched across the full dynamic range of the image.

the sum is over all pixels i,j in the image, V_{IN} denotes the input displacement field, and V_{OUT} denotes the recovered displacement field. This standard deviation indicates the accuracy of each PIV field for different R_1 and R_2 distances.

IV. PIV RESULTS FROM SIMULATED PHASE CONTRAST IMAGES

PIV analysis is performed using the simulated phase-contrast images (Figs. 6 and 7) of the mouse lung. In order to optimize the in-line phase-contrast imaging system for PIV analysis, PIV performance on phase contrast images as a function of imaging geometry and parameters is studied.

A. Effect of phase contrast on PIV

In Fig. 6(a1), the simulated absorption contrast image of the simulated mouse lung shows low contrast. This contact image corresponds to $R_2 = 0$ m. A phase contrast image of the same sample at $R_2 = 1$ m (Fig. 6(c1)) shows a significant improvement of contrast level, by a factor of 300.

As shown in Fig. 6(a), the SNR of the correlation peak of the absorption contrast image drops to the background noise level. As no correlation peak from the absorption contrast image is obtained, in this case PIV fails to estimate the displacement of the alveoli from the absorption images.

In contrast, the displacement of the simulated air spheres is successfully estimated by the sharp correlation peak (Fig. 6(b2)) from the speckle patterns. The diminution of the photon flux captured by the detector increases the noise level of the image (Fig. 6(c1)). Here, the SNR of the cross-correlation peak with noise (Fig. 6(c2)) is almost as high as that of the noise-free correlation peak (Fig. 6(b2)), demonstrating that for the simulations presented here the effect of light diminution and associated noise in the phase-contrast data only implies a minor impact on the accuracy of phase contrast PIV. Moreover, the fact that PIV fails to provide displacement estimation from the absorption-contrast data suggests that the presence phase-contrast for performing PIV on lung tissue is beneficial.

B. Effect of changing R_1 and R_2

The source-object distance R_1 and the object-detector distance R_2 play different roles in the detected phase-contrast image due to a laboratory source. To determine the

importance of tuning R_1 and R_2 in the context of optimizing laboratory-based x-ray phase-contrast velocimetry reconstruction, three sets of R_1 and R_2 distances have been chosen to generate phase-contrast images to investigate the effect of each distance on the final PIV result (Fig. 7).

The phase-contrast image for $R_1 = 1\,m$ and $R_2 = 1.5\,m$ (Fig. 7(a1)) has the lowest PIV-error of the three cases, with a correlation peak of the highest SNR ratio 9.43 (Fig. 7(a2)). By decreasing R_2 to 0.3 m (Fig. 7(b1)), the shortened propagation distance results in a lower detected phase-contrast level ($\kappa = 0.47\%$), the image has a noise-like high spatial frequency component. The correlation peak of this case has the lowest SNR (Fig. 7(b2)), implying that the PIV-error at this distance is the highest among the three cases. Increasing R_1 to 1.8 m (Fig. 7(c1)) has a minor effect on the phase-contrast pattern when compared with the pattern shown in Fig. 7(a1), the phase-contrast level at this distance is the lowest ($\kappa = 0.13\%$) due to the large divergence of the x-ray beam; however, the SNR of the correlation peak (Fig. 7(c2)) is higher than that of Fig. 7(b2); this suggests that the sample-detector distance R_2 plays a more important role than the source-object distance R_1 in phase-contrast PIV of laboratory-based source.

Note the phase-contrast level of the images in the left column of Fig. 7. Reducing R_2 from 1.5 m (Fig. 7(a1)) to
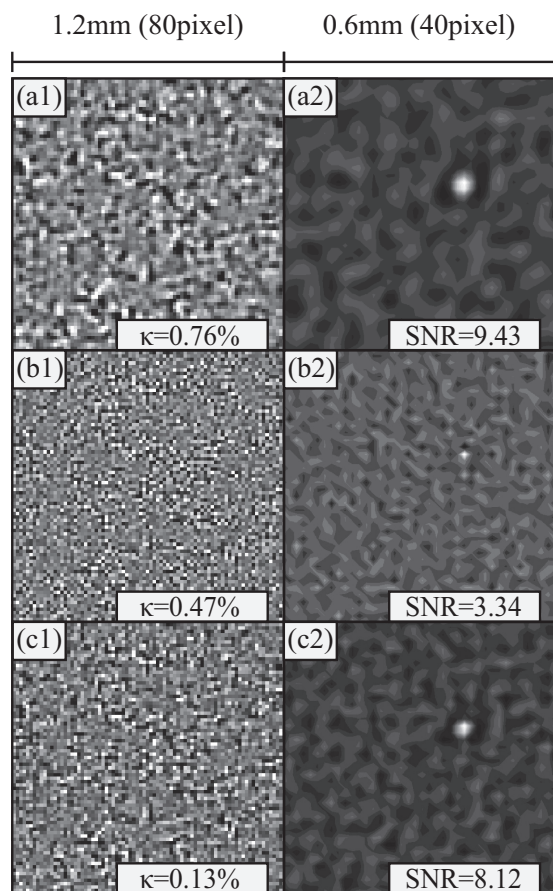
0.3 m (Fig. 7(b1)) reduces the size of the speckles, the noise-like speckle pattern has a greater proportion of optical power at $R_2 = 0.3\,m$ compared to the speckles in Fig. 7(a1), and phase-contrast is reduced accordingly. On the other hand, increasing R_1 would also reduce the contrast level due to the associated reduction in the photon flux incident on the sample as found in Fig. 7(c1). Therefore, the contrast level can be reduced both by decreasing R_2 to reduce phase-contrast and by increasing R_1 to reduce incident x-ray photon flux. Simulation results show that the PIV-error remains low even when the photon flux of incident x-ray is low, as found in the correlation peak in Fig. 7(c2). This fact suggests that in phase-contrast PIV for lung tissue, the detected contrast level κ of the image is not the only criterion to correlate with the accuracy of the PIV result.

C. Effect of effective pixel size and source size

The simulation accounts for the detector's effective pixel size, namely the pixel size of all image data after it has been referred back to the exit-surface of the sample, which provides a lower bound on the spatial resolution of the phase-contrast image. This is done by spatially binning the phase-contrast images at a variety of different levels. Binning has been performed to give images of 5, 10, 15, 20, 25, and 30 μm pixel size. The PIV-error at each distance pair is determined, Figs. 8 and 9 show the PIV-error as a contour map as a function of R_1 and R_2.

The optimal distance occurs at regions of dark contour level. As binning level increases, this optimal region shifts toward the higher R_2 region. The effect of source blurring is diminished by a larger effective pixel size; however, a longer propagation distance is required to generate diffraction fringes which are sufficiently broad to be detectable at the lower spatial resolution.

For solid target microfocus sources, photon flux is typically proportional to the diameter of the source. For our study, subject to the simplifying assumption that the total number of photons per unit time emitted from the source is directly proportional to the area of the source, increasing the source size shifts the optimal distance to the regions of low R_2 (Fig. 9). This is because increasing the source size strengthens the degree to which penumbral blurring degrades the propagation-based phase contrast images.

At the top left region of each error-map in Figs. 8 and 9, a high PIV-error region is observed. This region has the highest R_2/R_1 ratio and hence the largest penumbral blurring width $\Delta \approx D(R_2/R_1)$. Therefore, the PIV-error in this region is increased by the effect of penumbral blurring. The relative effect of edge blurring of the image is reduced relative to the increasing of pixel size as shown in Fig. 8. Reduction of penumbral blurring can also be achieved by reducing source size as shown in Fig. 9.

The other high PIV-error region is found at the bottom right region of each map. This region of high PIV-error is due to the low level of phase contrast and the low x-ray photon flux. In the case of 5 μm pixel in Fig. 8, photon flux at the bottom right region was insufficient to generate phase contrast image with detectable SNR. The SNR of the image
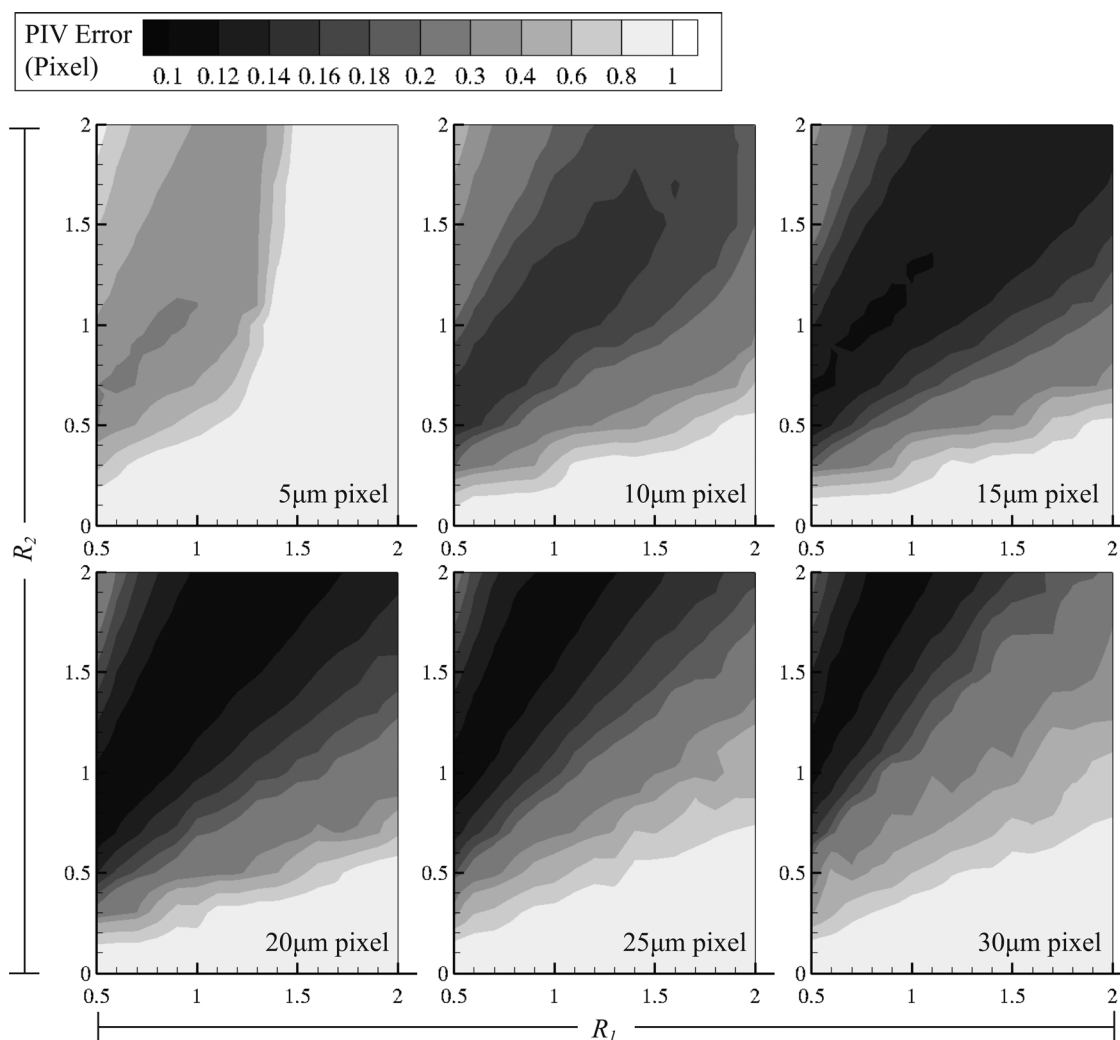
1.2mm (80pixel)	0.6mm (40pixel)

FIG. 7. Phase-contrast images (left column) and the corresponding correlation peaks (right column) at the distance of (a) $R_1 = 1\,m$, $R_2 = 1.5\,m$; (b) $R_1 = 1\,m$, $R_2 = 0.3\,m$; (c) $R_1 = 1.8\,m$, $R_2 = 1.5\,m$. Note that in panels (a1), (b1), and (c1) the intensity has been stretched across the full dynamic range of the image.

FIG. 8. Contour maps of PIV-error as a function of R_1 and R_2. Effective pixel size of 5, 10, and 15 μm (top: left to right) and 20, 25, and 30 μm (bottom: left to right). The PIV-error is determined as the normalized root mean square error between the known vortical displacement field and the reconstruction of this field obtained using phase-contrast PIV. In the simulations represented by all six error-maps, the source size was kept constant at 20 μm.

can be increased by increasing the pixel size as shown in the case of 10 μm pixel in Fig. 8. However, as indicated in Fig. 7(b1), speckle patterns at this low R_2 region have a high spatial frequency. Imaging systems with low spatial resolution are insufficient to resolve the speckle patterns. As shown in Fig. 8, PIV-error at the bottom right region increases from the 10 μm pixel to the 30 μm pixel. Stronger phase-contrast (i.e., longer R_2) is required to generate speckles with wider average size to overcome the low resolution of the camera. This source of PIV-error can be reduced by using a large x-ray source as shown in Fig. 9. The higher photon flux of the incident x-ray beam increases the signal-to-noise level of the image; this reduces the R_2 distance required to generate sufficient phase-contrast.

D. Relationship between geometric magnification and PIV accuracy

In the twelve PIV-error-maps of different effective pixel size and source size (Figs. 8 and 9), the contour of constant PIV-error shows an approximate linear relationship with R_1 and R_2, regardless of the pixel size and the source size. A

function of R_1 and R_2 is suggested to be the key indication of PIV-error.

Results for the measurement of the PIV accuracy and the geometric magnification obtained in systems with different source size and pixel size (Fig. 10) show that the PIV-error contour and the corresponding lines of constant geometric magnification have a high level of agreement. This suggests that the PIV-error is approximately constant for a given level of geometric magnification $M = (R_1 + R_2)/R_1$.

As shown in Fig. 10, the degree of matching between the contour and the lines increases as the magnification increases. Phase-contrast images have a larger degree of optical power at high spatial frequencies at low geometric magnification. However, the noise-like images introduce instability in the PIV-error; hence, the agreement between the magnification lines and the error contour is lower at low magnification.

The high level of agreement between the geometric magnification lines and the PIV-error contour shown in Fig. 10 suggests that phase-contrast PIV-error is a function of the geometric magnification of the imaging system. For each given pixel size and source size in Figs. 8 and 9, the
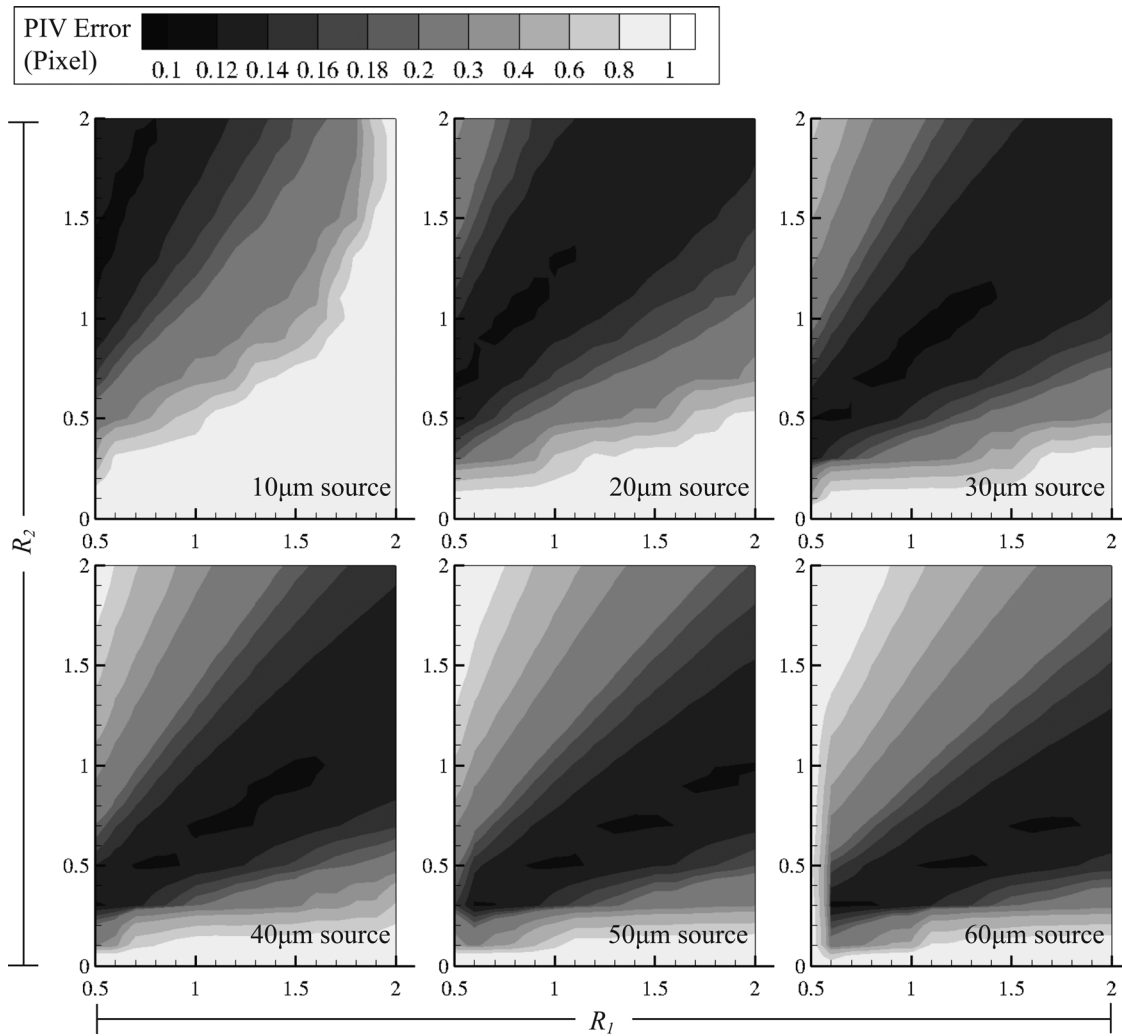
FIG. 9. Contour maps of PIV-error as a function of R_1 and R_2. Source size of 10, 20, and 30 μm (top: left to right) and source size of 40, 50, and 60 μm (bottom: left to right). In the simulations represented by all six error-maps, the pixel size was kept constant at 15 μm.
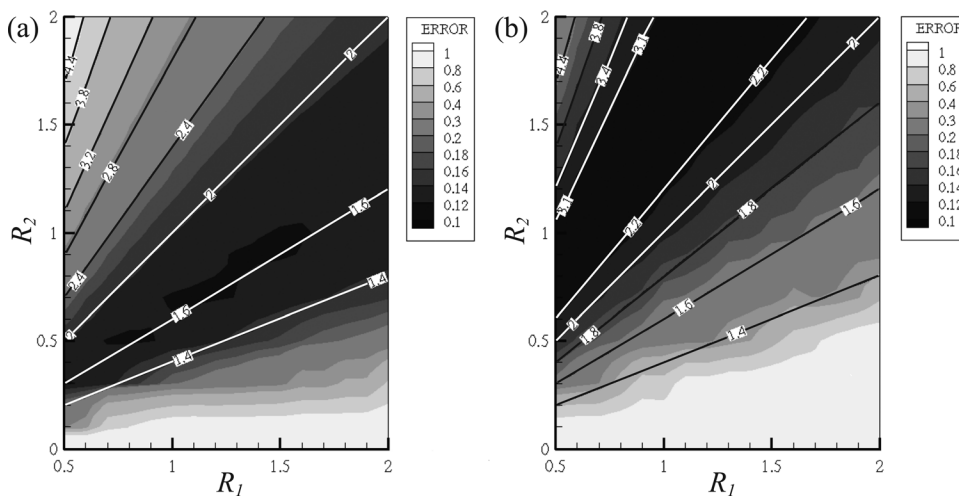

FIG. 10. PIV-error-maps of 40 μm source (a) and 20 μm pixel size (b). Contour indicates the PIV-error, solid lines (in black or white) overlapping the contour indicate the corresponding magnification.

PIV-error is plotted against the geometric magnification and results are shown in Figs. 11 and 12. The multivalued curves found in the 5 μm pixel case in Fig. 11 and in the 10 μm source case in Fig. 12 are due to the under-exposure of the weak incident x-ray (i.e., the utilization of only a small portion of the available dynamic range of the simulated detec-

tor). Similar features are also obtained in the 50 and 60 μm source cases in Fig. 12, these curves are due to the over-exposure of the intense incident x-rays (i.e., clipping of the high intensity regions of the image data due to the signal in certain pixels exceeding the dynamic range of the detector). Ignoring the factor of under-exposure and over-exposure,
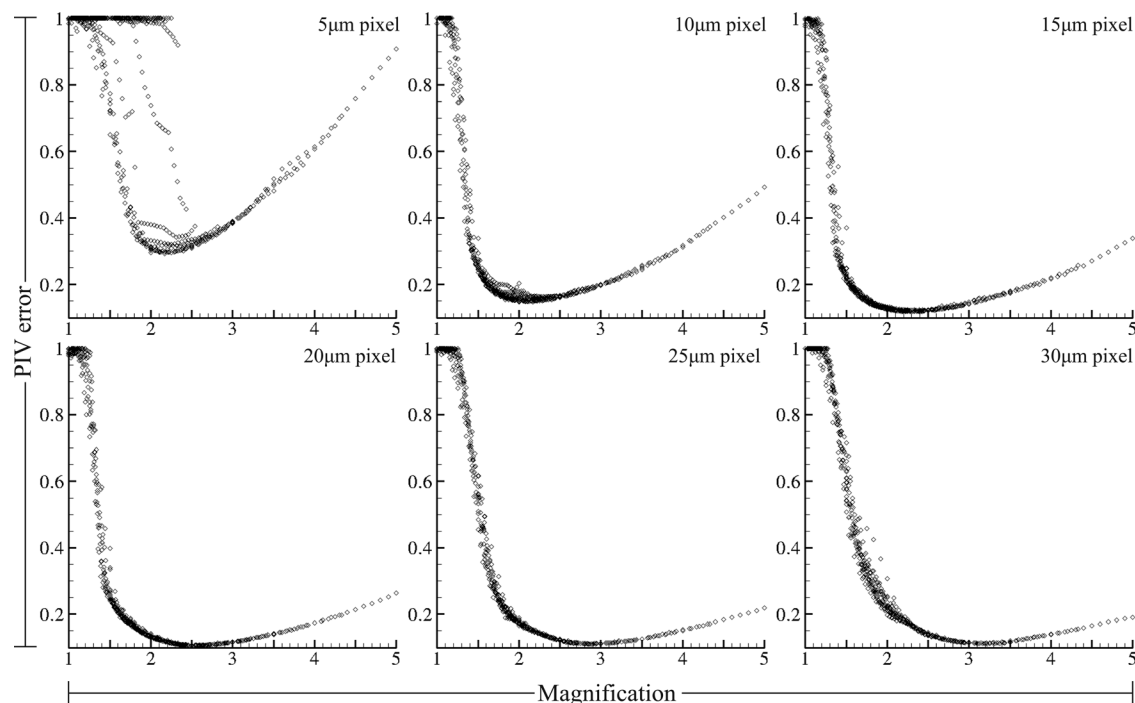
FIG. 11. Plots of PIV-error versus magnification with different defective pixel size. Top (left to right): effective pixel sizes of 5, 10, and 15 μm; bottom (left to right): effective pixel sizes of 20, 25, and 30 μm. The source size was kept constant at 20 μm for all six plots.

results in Figs. 11 and 12 further suggest that the accuracy of phase-contrast PIV can be expressed as a function of geometric magnification.

Note that at magnification $M = 1$, the PIV-error in all figures is always the highest. This magnification occurs at $R_2 = 0$, again suggesting that phase-contrast is essential for performing PIV of lung movement. Pure absorption contrast would fail to provide enough contrast for particle correlations in PIV.

E. Optimization of in-line phase contrast PIV for a lab-source system

Results in Fig. 11 show that the PIV-error remains low (<0.2 pixel) for large pixel size ($>15\,\mu$m) at a wider range of magnification. This suggests that for imaging systems with large effective pixel size, the PIV accuracy is relatively insensitive to the change of R_1 and R_2 when compared to the systems with smaller effective pixel size. This consistency of
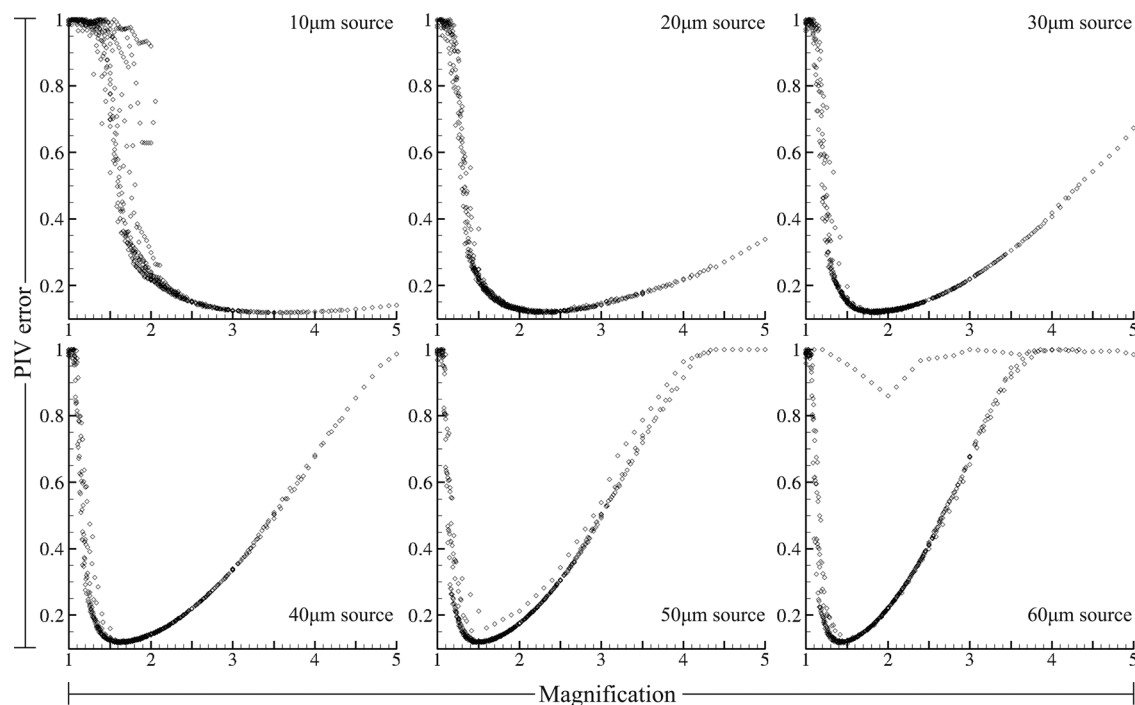

FIG. 12. Plots of PIV-error versus magnification with different source size. Top (left to right): source sizes of 10, 20, and 30 μm; bottom (left to right): source sizes of 40, 50, and 60 μm. The pixel size was kept constant at 15 μm for all six plots.

PIV accuracy suggests that for in-line phase-contrast laboratory-source based system, large detector pixels can provide a higher degree of flexibility in the selection of R_1 and R_2 than that of small detector pixels.

Note that the PIV-error curves in Figs. 11 and 12 "bottom out" at limiting values on the order of 0.1. This limiting value is a well-known practical limit to the PIV sub-pixel interpolation scheme. A general discussion on the errors in PIV analysis can be found in Huang *et al.*[35] and a more specific discussion of the PIV algorithms used here and their associated errors can be found in Fouras *et al.*[30,31]

On the other hand, results in Fig. 12 show that the optimal PIV imaging configuration is restricted into a small range of magnification for systems with large source size.

Large source size D introduces large penumbral blurring to the imaging system. The penumbral blurring width $\Delta \approx D(R_2/R_1)$ for systems with large source size increases rapidly as geometric magnification M increases. As PIV accuracy becomes highly sensitive to the R_2/R_1 ratio, the selection of R_1 and R_2 is less flexible for such systems. However, the required magnification M for the large-source systems is generally smaller than that of the systems with large detector pixels. For a system with large detector pixels

(effective pixel size greater than 15 μm as shown in Fig. 11), the optimal magnification is generally greater than 2.5, while for a large-source system (source size greater than 30 μm), this optimal magnification is smaller than 1.5. This suggests that a system with a shorter total length can be achieved by using a large source as seen in Fig. 13, where the trends are obtained from the optimal magnifications for phase-contrast PIV from Figs. 11 and 12.

The general approach to optimize phase contrast imaging is that a small source size and a high spatial resolution detector can improve the imaging quality.[10,28,36] By comparison with this point of view, plots in Figs. 11 and 12 show that large pixel size and source size can provide the same level of or even improve the accuracy of PIV estimation if the magnification is optimized.

V. CONCLUSION

Investigation of the contrast level of images and the corresponding correlation peaks suggests that PIV optimization is distinct from phase-contrast optimization. In optimizing the accuracy of PIV measurement for a laboratory source x-ray phase-contrast system, from our simulation of systems with a maximum source-detector distance of 4 m, results suggest that one can simplify the optimization of the system by optimizing the geometric magnification. For large effective pixel size (>15 μm), systems with high geometric magnification (>2.5) are desired. For large source sizes (>30 μm), low magnification (<1.5) with resultant smaller pixel sizes at the detector would be suggested instead. In practice, these results suggest that the total required length of a phase contrast PIV system is proportional to the effective pixel-size of the detector in the system, while systems with large pixel size have the advantage of high flexibility of R_1 and R_2 selection. This is particularly useful for PIV imaging in which pixel-binning is commonly be used in order to increase the signal-to-noise ratio. On the other hand, the total length of the system can be reduced by using a large source, at the expense of a higher resolution detector and a loss of the flexibility of R_1 and R_2 selection. Our model suggests that by adjusting the geometric magnification of the system, the same level of accuracy of PIV measurement can be achieved for systems with various source sizes and pixel sizes. This suggests a large degree of flexibility in the selection of source and detector for experiments of phase contrast x-ray PIV using laboratory sources. Results also show that for absorption contrast, PIV-error is always higher than that of the corresponding phase contrast scenario, suggesting that phase contrast is indeed essential for the model sample used in this study (based on lung tissue) for practical velocimetry.
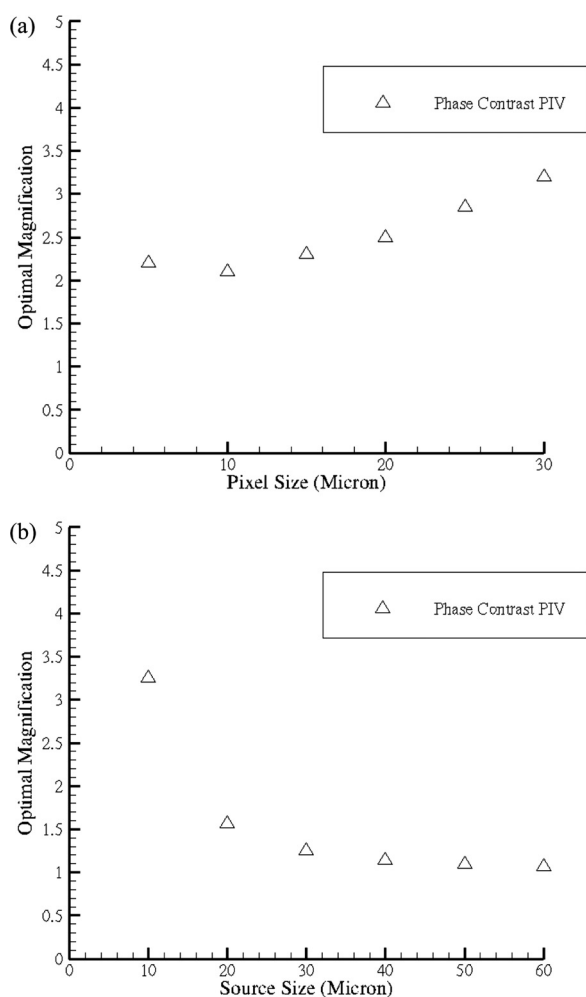

FIG. 13. Plots of optimal magnification for phase-contrast PIV versus (a) pixel size; (b) source size. Data for phase-contrast PIV in (a) and (b) are obtained from Figs. 11 and 12, respectively.

[1]W. C. Röntgen, Nature **53**, 274 (1896).
[2]C. A. Helms, *Fundamentals of Skeletal Radiology*, 3rd ed. (Elsevier, Philadelphia, USA, 2003).
[3]E. D. Pisano, M. J. Yaffe, and C. M. Kuzmiak, *Digital Mammography* (Lippincott Williams & Wilkins, Philadelphia, USA, 2004).
[4]A. Momose, T. Takeda, Y. Itai, and K. Hirano, Nat. Med. **2**, 473 (1996).
[5]R. Alford, H. M. Simpson, J. Duberman, G. C. Hill, M. Ogawa, C. Regino, H. Kobayashi, and P. L. Choyke, Mol. Imaging **8**(6), 341 (2009).
[6]A. Snigirev, I. Snigireva, V. Kohn, S. Kuznetsov, and I. Schelokov, Rev. Sci. Instrum. **66**(12), 5486 (1995).
[7]P. Cloetens, R. Barrett, J. Baruchel, J. P. Guigay, and M. Schlenker, J. Phys. D: Appl. Phys. **29**, 133 (1996).
[8]K. A. Nugent, T. E. Gureyev, D. F. Cookson, D. Paganin, and Z. Barnea, Phys. Rev. Lett. **77**, 2961 (1996).
[9]S. W. Wilkins, T. E. Gureyev, D. Gao, A. Pogany, and A. W. Stevenson, Nature **384**, 335 (1996).
[10]T. E. Gureyev, S. C. Mayo, D. E. Myers, Ya. Nesterets, D. M. Paganin, A. Pogany, A. W. Stevenson, and S. W. Wilkins, J. Appl. Phys. **105**, 102005 (2009).
[11]R. J. Adrian, Exp. Fluids **39**, 159 (2005).
[12]M. Raffel, C. Willert, S. T. Wereley, and J. Kompenhans, *Particle Image Velocimetry: A Practical Guide*, 2nd ed. (Springer, Berlin, 2007).
[13]A. Fouras, J. Dusting, R. Lewis, and K. Hourigan, J. Appl. Phys. **102**, 064916 (2007).
[14]S. J. Lee and G. B. Kim, J. Appl. Phys. **94**, 3620 (2003).
[15]A. Fouras, M. J. Kitchen, S. Dubsky, R. A. Lewis, S. B. Hooper, and K. Hourigan, J. Appl. Phys. **105**, 102009 (2009).
[16]S. C. Irvine, D. M. Paganin, R. A. Jamison, S. Dubsky, and A. Fouras, Opt. Express **18**, 2368 (2010).
[17]A. Fouras, J. Dusting, J. Sheridan, M. Kawahashi, H. Hirahara, and K. Hourigan, Clin. Exp. Pharmacol. Physiol. **36**, 238 (2009).
[18]R. A. Jamison, S. Dubsky, K. K. W. Siu, K. Hourigan, and A. Fouras, Ann. Biomed. Eng. **39**, 1643 (2011).
[19]A. Seeger, K. Affeld, L. Goubergrits, E. Wellnhofer, and U. Kertzscher, Exp. Fluids **31**, 193 (2001).
[20]S. Dubsky, R. A. Jamison, S. C. Irvine, K. K. W. Siu, K. Hourigan, and A. Fouras, Appl. Phys. Lett. **96**, 023702 (2010).
[21]A. Fouras, B. J. Allison, M. J. Kitchen, S. Dubsky, J. Nguyen, K. Hourigan, K. K. W. Siu, R. A. Lewis, M. J. Wallace, and S. B. Hooper, Ann. Biomed. Eng. **40**, 1160 (2012).
[22]F. E. Carroll, M. H. Mendenhall, R. H. Traeger, C. Brau, and J. W. Waters, Am. J. Roentgenol. **181**, 1197 (2003).
[23]U. Bonse and M. Hart, Appl. Phys. Lett. **6**, 155 (1965).
[24]F. Pfeiffer, M. Bech, O. Bunk, P. Kraft, E. F. Eikenberry, Ch. Brönnimann, C. Grünzweig, and C. David, Nature Mater. **7**, 134 (2008).
[25]C. Kottler, F. Pfeiffer, O. Bunk, C. Grünzweig, J. Bruder, R. Kaufmann, L. Tlustos, H. Walt, I. Briod, T. Weitkamp, and C. David, Phys. Status Solidi **204**, 2728 (2007).
[26]S. C. Mayo, P. R. Miller, S. W. Wilkins, T. J. Davis, D. Gao, T. E. Gureyev, D. Paganin, D. J. Parry, A. Pogany, and A. W. Stevenson, J. Microsc. **207**, 79 (2002).
[27]B. D. Arhatari, K. Hannah, E. Balaur, and A. G. Peele, Opt. Express **16**, 19950 (2008).
[28]Y. S. Kashyap, P. S. Yadav, T. Roy, P. S. Sarkar, M. Shukla, and A. Sinha, Appl. Radiat. Isot. **66**, 1083 (2008).
[29]D. Paganin, *Coherent X-ray Optics* (Oxford University Press, New York, USA, 2006).
[30]A. Fouras, J. Dusting, and K. Hourigan, Exp. Fluids **42**, 799 (2007).
[31]A. Fouras, D. Lo Jacono, and K. Hourigan, Exp. Fluids **44**, 317 (2008).
[32]M. J. Kitchen, D. Paganin, R. A. Lewis, N. Yagi, K. Uesugi, and S. T. Mudie, Phys. Med. Biol. **49**, 4335 (2004).
[33]M. Sánchez del Río and R. J. Dejus, "XOP 2.1: A new version of the X-ray optics software toolkit" in Eighth International Conference on Synchrotron Radiation Instrumentation (Americal Institute of Physics, 2004), p. 784.
[34]M. Born and E. Wolf, *Principles of Optics* (Cambridge University Press, 1997).
[35]H. Huang, D. Dabiri, and M. Gharib, Meas. Sci. Technol. **8**, 1427 (1997).
[36]Ya. I. Nesterets, S. W. Wilkins, T. E. Gureyev, A. Pogany, and A. W. Stevenson, Rev. Sci. Instrum. **76**, 093706 (2005).